Convective heat transport in compressible fluids

Akira Furukawa and Akira Onuki
Department of Physics, Kyoto University, Kyoto 606-8502, Japan
(Received 1 February 2002; published 18 July 2002)

We present hydrodynamic equations of compressible fluids in gravity as a generalization of those in the Boussinesq approximation used for nearly incompressible fluids. They account for adiabatic processes taking place throughout the cell (the piston effect) and those taking place within plumes (the adiabatic temperature gradient effect). Performing two-dimensional numerical analysis, we reveal some unique features of plume generation and convection in transient and steady states of compressible fluids. As the critical point is approached, the overall temperature changes induced by plume arrivals at the boundary walls are amplified, giving rise to overshoot behavior in transient states and significant noise in the temperature in steady states. The velocity field is suggested to assume a logarithmic profile within boundary layers. Random reversal of macroscopic shear flow is examined in a cell with unit aspect ratio. We also present a simple scaling theory for moderate Rayleigh numbers.

DOI: 10.1103/PhysRevE.66.016302 PACS number(s): 44.25.+f, 47.27.Te, 64.70.Fx

I. INTRODUCTION

Recently much attention has been paid to organized fluid motion in turbulent convection in the Rayleigh-Bénard geometry [1–7]. Although the conventional hydrodynamic equations are constructed for (nearly) incompressible fluids [8], we may mention a number of convection experiments in compressible one-component fluids in the supercritical region [9–19], together with those in noncritical fluids such as water or Hg [20–22]. In these studies the Nusselt number Nu representing the efficiency of convective heat transport has been measured at large values of the Rayleigh number Ra defined by

$$\mathrm{Ra}=\alpha_p\rho g L^3\Delta T/\eta D. \tag{1.1}$$

Here g is the gravity constant, $\Delta T=T_{\mathrm{bot}}-T_{\mathrm{top}}$ is the difference between the bottom and top temperatures, and L is the cell height. As the critical point is approached in one-component fluids, the thermal expansion coefficient $\alpha_p=-(\partial\rho/\partial T)_p/\rho$ grows strongly as $\xi^{\gamma/\nu}$ (in the same manner as the isothermal expansion coefficient K_T and the isobaric specific heat C_p), the thermal diffusivity D decreases as ξ^{-1}, and the shear viscosity η is nearly a constant. Here ξ is the thermal correlation length growing as $(T/T_c-1)^{-\nu}$ on the critical isochore with $\gamma\cong 1.24$ and $\nu\cong 0.625$. Hence, in the critical region, Ra can be extremely large; for example, Ra $\sim 10^{13}$ even for not very long $L(\lesssim 10$ cm). The Prandtl number $\mathrm{Pr}=\eta/\rho D$ was in the range of 1–100.

High compressibility of supercritical fluids gives rise to some unique features not encountered in incompressible fluids.

(i) First, the transient behavior after application of a heat flux from the bottom is strongly influenced by the so-called piston effect [23–30], as revealed by recent high-precision experiments on ^{3}He [17] and reproduced by subsequent simulation [31].

(ii) Second, as α_p grows, the usual mechanism of convection onset $\mathrm{Ra}>\mathrm{Ra}_c(\cong 1708)$ is replaced by that of the Schwarzschild criterion [32,33]. That is, for large compressible fluid columns (even far from the critical point), convection sets in when thermal plumes continue to rise upward adiabatically. This occurs when the applied temperature gradient $|dT/dz|$ is larger than the adiabatic gradient [34],

$$a_g=(\partial T/\partial p)_s\rho g, \tag{1.2}$$

which is equal to 0.034 mK/cm for ^{3}He and 0.27 mK/cm for CO_2. This is the condition that the entropy $s=s(T,p)$ per unit mass decreases with height as $ds/dz=(C_p/T)[dT/dz+a_g]<0$, under which the entropy of fluid elements adiabatically convected upward is larger than that of the ambient fluid. More precisely, Gitterman and Steinberg [32] found that the convection onset for compressible fluids is given by $\mathrm{Ra}^{\mathrm{corr}}>\mathrm{Ra}_c$, where $\mathrm{Ra}^{\mathrm{corr}}$ is a corrected Rayleigh number defined by

$$\mathrm{Ra}^{\mathrm{corr}}=(\alpha_p\rho g L^3/\eta D)(\Delta T-a_g L)=\mathrm{Ra}(1-a_g L/\Delta T). \tag{1.3}$$

This is a natural consequence because the effective temperature gradient seen by the raising plumes is given by $\Delta T/L-a_g$. At the convection onset we thus have

$$(\Delta T)_{\mathrm{on}}=a_g L+\mathrm{Ra}_c D\,\eta_0/(g\rho\alpha_p L^3), \tag{1.4}$$

as was confirmed in SF_6 [11] and in ^{3}He [16]. In Eq. (1.4) the ratio of the first to the second term behaves as $L^4/(T/T_c-1)^{\gamma+\nu}$ and can exceed 1 as $T\to T_c$ even for small L. In the experiment on ^{3}He [16] this was the case in the range $T/T_c-1\lesssim 0.05$ for $L\sim 1$ mm.

(iii) Third, in steady convective states, experimental curves of Ra (Nu-1) vs $\mathrm{Ra}^{\mathrm{corr}}$ were collapsed onto a single universal curve for various densities and above T_c [12] and for various average reduced temperatures on the critical isochore [16]. These empirical results are highly nontrivial, because Nu can in principle depend on Ra, Pr, and $a_g L/\Delta T$, while Nu is a function of Ra and Pr for incompressible fluids, neglecting the effects of confinement.

For various fluids under a relatively large $\Delta T \gg a_g L$ (where $\mathrm{Ra}^{\mathrm{corr}} \cong \mathrm{Ra}$), data of $\mathrm{Nu} = QL/\lambda \Delta T$ have been fitted to a simple scaling law,

$$\mathrm{Nu} \sim \mathrm{Ra}^a, \tag{1.5}$$

where Q is the heat flux and λ is the thermal conductivity. The exponent a has been in a range from 0.28 to 0.31 and, in particular, a theoretical value 2/7 [2,4] was generally consistent with data for $\mathrm{Ra} \lesssim 10^{12}$ [9–18,21]. Moreover, measurements of the patterns of isothermal surfaces [20] and the velocity [21,22] have been informative on plume motion and a large-scale circulating shear flow in small-aspect-ratio cells [19,21]. Several authors have also performed numerical analysis of convection at large Ra in two dimensions (2D) [35–39] and in three dimensions (3D) [40–43]. Even in 2D salient features in the experiments have been reproduced. In these simulations, if the temperature is averaged over a long time, the temperature gradient is localized in thin boundary layers with thickness ℓ_T related to Nu by

$$\mathrm{Nu} = L/2\ell_T. \tag{1.6}$$

Both in 2D and in 3D (if visualized from side), the plumes tend to be connected from bottom to top for large Pr because of slow thermal diffusion, while they become diffuse far from the boundaries for small Pr. In the 3D simulations with periodic or free-slip sidewalls [42,43], local boundary shear flows were observed between incoming plumes and outgoing networks of buoyant sheets in horizontal planes close to the boundaries.

In this paper we will derive and examine hydrodynamic equations for compressible fluids under gravity in the supercritical region, in which the oscillatory motion of sound has been averaged out [23]. Since the time scale of convective motions is much longer than that of the acoustic wave $t_{\mathrm{ac}} = L/c$ (typically of order 10^{-4} s for $L \sim 1$ cm), such a description is convenient theoretically and is even indispensable for numerical analysis. Our dynamic equations are a natural generalization of the usual hydrodynamic equations [8]. Our new predictions are unique particularly when the piston effect comes into play, as has been demonstrated in the previous simulation [31] relatively close to the convection onset. This paper will present 2D simulations of our hydrodynamic equations for much larger $\mathrm{Ra}^{\mathrm{corr}}$ both in transient and (dynamical) steady states. Even in steady states, we will find some characteristic features of turbulent states, which have not been reported in the previous simulations [35–37,40–43], such as the logarithmic velocity profile of the velocity near the boundary [34] and random reversal of the large-scale circulating flow in small-aspect-ratio cells [19,21]. We will also point out that individual arrivals of plumes at the boundaries cause global temperature fluctuations in the cell via the piston effect. The resultant noise level of the temperature fluctuations grows as the critical point is approached.

II. THEORETICAL BACKGROUND

A. Hydrodynamic equations

We consider a supercritical fluid on the critical isochore in a cell with the bottom plate at $z=0$ and the top plate at $z=L$. The z axis is taken in the upward direction and the total fluid volume is fixed at V. The temperature disturbance $\delta T(\boldsymbol{r},t) = T(\boldsymbol{r},t) - T_{\mathrm{top}}$ measured from the temperature T_{top} at the top boundary is much smaller in magnitude than $T_{\mathrm{top}} - T_c$. Hereafter ϵ will be used to denote the reduced temperature at the top boundary, which satisfies

$$\epsilon = T_{\mathrm{top}}/T_c - 1 \gg \Delta T/T_c. \tag{2.1}$$

We assume that the gravity-induced density stratification is not too severe such that the thermodynamic derivatives are nearly homogeneous in the cell. This is satisfied when $|\rho/\rho_c - 1| \sim (\partial\rho/\partial p)_T g L \ll \epsilon^\beta$ with $\beta \cong 0.33$ [44]. This condition is rewritten as

$$\epsilon^{\beta+\gamma} \gg a_g L/T_c. \tag{2.2}$$

In the theoretical literature on convection [2–7], the top and bottom temperatures T_{bot} and T_{top} are constant parameters. However, in most of the recent convection experiments, especially where the heat transport is to be measured, the heat flux at the bottom $Q = -\lambda (dT/dz)_{z=0}$ and T_{top} have been fixed. Furthermore, if the top and bottom walls are made of a metal with high thermal conductivity, the boundary temperatures become homogeneous in the lateral directions (unless local temperature changes are too fast). Then $T_{\mathrm{bot}}(t)$ and hence $\Delta T(t)$ are functions of time only. This idealization is more justified under cryogenic conditions than at room temperatures, because the relative conductivity of the plates is much greater at low temperatures. Metcalfe and Behringer [45] performed linear stability analysis of convection onset under this fixed-heat-flux boundary condition. In the nonlinear regime, it is of great interest how the boundary condition influences the boundary layer thickness, the plume generation, and the boundary shear flow.

In equilibrium the pressure gradient is given by $-\rho g \cong -\rho_c g$. In nonequilibrium we set

$$p(\boldsymbol{r},t) = p_0 - \rho_c g z + p_1(t) + p_{\mathrm{inh}}(\boldsymbol{r},t), \tag{2.3}$$

where p_0 is a constant, $p_1(t)$ and p_{inh} are the homogeneous and inhomogeneous parts induced by δT, respectively. That is, we assume $\langle p_{\mathrm{inh}} \rangle = 0$, where $\langle \cdots \rangle \equiv \int d\boldsymbol{r} (\cdots)/V$ represents the space average in the cell. Then p_1 is related to the space average of δT by

$$p_1(t) = (\partial p/\partial T)_\rho \langle \delta T \rangle (t), \tag{2.4}$$

which follows from the thermodynamic relation $dp = (\partial p/\partial T)_\rho dT + (\partial p/\partial \rho)_T d\rho$ and the condition that the space average of the density deviation vanishes ($\langle \delta\rho \rangle = 0$). It is important that the combination $p(\boldsymbol{r},t) + \rho_c g z$ is nearly homogeneous or $|p_1(t)| \gg |p_{\mathrm{inh}}(\boldsymbol{r},t)|$ for fluid motions much slower than the acoustic time $t_{\mathrm{ac}} = L/c$ ($c \sim 10^4$ cm/s being the sound velocity) [23,24,46].

Now we derive the equation for δT from the heat conduction equation

$$\rho T\left(\frac{\partial}{\partial t}+\boldsymbol{v}\cdot\boldsymbol{\nabla}\right)s=\lambda\boldsymbol{\nabla}^2\delta T, \tag{2.5}$$

where $s(\boldsymbol{r},t)$ is the entropy per unit mass. Here it consists of the equilibrium part $s_{\rm eq}(z)$ with

$$\frac{d}{dz}s_{\rm eq}(z)=-\left(\frac{\partial s}{\partial p}\right)_T\rho g=T^{-1}C_p a_g \tag{2.6}$$

and the nonequilibrium deviation,

$$\delta s(\boldsymbol{r},t)=T^{-1}C_p\left[\delta T(\boldsymbol{r},t)-\left(\frac{\partial T}{\partial p}\right)_s p_1(t)\right]. \tag{2.7}$$

With the aid of the thermodynamic identity $(\partial T/\partial p)_s=(\partial T/\partial p)_\rho(1-1/\gamma_s)$, we rewrite Eq. (2.5) to obtain the desired equation for δT,

$$\left(\frac{\partial}{\partial t}+\boldsymbol{v}\cdot\boldsymbol{\nabla}-D\boldsymbol{\nabla}^2\right)\delta T=-a_g v_z+\alpha_s\frac{d}{dt}\langle\delta T\rangle, \tag{2.8}$$

where $D=\lambda/C_p$ is the thermal diffusivity and

$$\alpha_s=1-\gamma_s^{-1}. \tag{2.9}$$

The specific-heat ratio γ_s behaves as

$$\gamma_s=C_p/C_V\sim\epsilon^{-\gamma+\alpha}\gg 1, \tag{2.10}$$

where $C_p\sim\epsilon^{-\gamma}$ and $C_V\sim\epsilon^{-\alpha}$ are the specific heats (per unit volume) at constant p and V, respectively, with $\alpha\cong 0.1$. The first term on the right-hand side of Eq. (2.8) arises from $ds_{\rm eq}/dz$. Inside plumes the temperature is adiabatically lowered if they go upward ($v_z>0$), or adiabatically increased if they go downward ($v_z<0$). In this way this term suppresses upward motion of warmer plumes from the bottom and downward motion of cooler plumes from the top, resulting in the Schwarzschild criterion of convection onset (the adiabatic temperature gradient effect). On the other hand, the second term arises from $p_1(t)$, leading to the piston effect [24]. It is worth noting that the space integral of Eq. (2.8) in the cell becomes

$$VC_V\frac{d}{dt}\langle\delta T\rangle=\lambda\int da\boldsymbol{n}\cdot\boldsymbol{\nabla}\delta T, \tag{2.11}$$

where use has been made of $\langle\boldsymbol{v}\rangle=\boldsymbol{0}$. The right-hand side represents the rate of heat supply from the boundary surface, where da is surface element and $\boldsymbol{n}$ is the outward surface normal. Its time-integration is the total heat supply expressed as $V\rho\langle\delta s\rangle$, resulting in

$$C_V\langle\delta T\rangle(t)=\rho\langle\delta s\rangle(t), \tag{2.12}$$

which also follows from Eq. (2.4) and the space average of Eq. (2.7). The appearance of C_V on the left-hand side of Eq. (2.12) is a natural consequence under the fixed volume condition. Notice that Eq. (2.7) can also be written as

$$\delta T(\boldsymbol{r},t)=\frac{\rho T}{C_p}\delta s(\boldsymbol{r},t)+\rho T\left[\frac{1}{C_V}-\frac{1}{C_p}\right]\langle\delta s\rangle(t). \tag{2.13}$$

This relation holds even in gravity if δs is the deviation of $s-s_{\rm eq}(z)$ as in Eq. (2.7). In addition, the density deviation $\delta\rho=\rho-\langle\rho\rangle$ is written in our approximation as

$$\delta\rho=\rho K_T g(z-L/2)-\rho\alpha_p(\delta T-\langle\delta T\rangle), \tag{2.14}$$

where $K_T=(\partial\rho/\partial p)_T/\rho$ and we have set $\langle\delta\rho\rangle=0$.

Since $C_p\gg C_V$ near the critical point, the homogeneous part of δT (second term) in Eq. (2.13) can easily dominate over the inhomogeneous part (first term) even when δs is localized near a heated wall. Indeed, if a thermal disturbance is produced within a thermal boundary layer with thickness ℓ near the boundary, the ratio of the homogeneous part ($\propto\langle\delta s\rangle$) to the localized inhomogeneous part ($\propto\delta s$) in Eq. (2.13) is of order $(\gamma_s-1)l/L$ where L is the characteristic system length. Temperature homogenization is achieved when $(\gamma_s-1)l\gg L$. By setting $\ell=(Dt_1)^{1/2}$ we obtain the time constant of this thermal equilibration (the piston time) in the form

$$t_1=L^2/D(\gamma_s-1)^2. \tag{2.15}$$

Next we consider the momentum equation for the velocity field $\boldsymbol{v}(\boldsymbol{r},t)$. On long time scales, sound waves decay to zero and the incompressibility condition

$$\boldsymbol{\nabla}\cdot\boldsymbol{v}=0 \tag{2.16}$$

becomes nearly satisfied ($\gg t_{\rm homo}$) [46]. Then the dissipation of $\boldsymbol{v}$ is produced by the shear viscosity η and the usual Navier-Stokes equation in the Boussinesq approximation may be set up in the form [1]

$$\left(\frac{\partial}{\partial t}+\boldsymbol{v}\cdot\boldsymbol{\nabla}\right)\boldsymbol{v}=-\boldsymbol{\nabla}\frac{p_{\rm inh}}{\rho}+\alpha_p g\,\delta T\boldsymbol{e}_z+\frac{\eta}{\rho}\boldsymbol{\nabla}^2\boldsymbol{v}, \tag{2.17}$$

where the inhomogeneous part $p_{\rm inh}$ ensures Eq. (2.16), $\boldsymbol{e}_z$ is the unit vector along the z axis, and $\rho(\cong\langle\rho\rangle)$ may be treated as the average density. The two equations (2.8) and (2.17) are our fundamental dynamic equations closed under Eq. (2.16). In the conventional theory [1,8], Eq. (2.17) has been used, but the right-hand side of Eq. (2.8) vanishes.

As another characteristic feature near the critical point, the Prandtl number behaves as

$$\mathrm{Pr}=\eta/\rho D\sim\epsilon^{-\nu}. \tag{2.18}$$

For example, $\mathrm{Pr}=350$ at $T/T_c-1=10^{-3}$ in ^{3}He. This means that the time scale of the thermal diffusion is much slower than that of the velocity in the critical region. Based on this fact, the simulation in Ref. [31] was performed using the Stokes approximation in which the left-hand side of Eq. (2.17) is set equal to zero. Good agreement with the experiments [17] was then obtained for $\mathrm{Ra}^{\rm corr}/\mathrm{Ra}_c-1\lesssim 5$ at $\epsilon=0.05$.

For $\mathrm{Pr}\gg 1$, let us estimate the upper bound of $\mathrm{Ra}^{\rm corr}$ below which the Reynolds number Re is smaller than 1 or the

Stokes approximation is allowable. The characteristic temperature variation $(\delta T)_\perp$ changing perpendicularly to the z axis and the characteristic velocity field $v_{\rm pl}$ are related by

$$v_{\rm pl}\sim(\alpha_p\rho_c g/\eta k^2)(\delta T)_\perp, \tag{2.19}$$

where $k\sim 2\pi/L$ for roll patterns. If $\mathrm{Ra}^{\rm corr}/\mathrm{Ra}_c$ is considerably (but not much) larger than 1, $(\delta T)_\perp/\Delta T$ is of order 1 (but somewhat smaller than 1). Then we obtain

$$v_{\rm pl}\sim(\mathrm{Ra}^{\rm corr}/\mathrm{Ra}_c)D/L. \tag{2.20}$$

Thus the small Reynolds number regime is written as

$$\mathrm{Ra}^{\rm corr}/\mathrm{Ra}_c\lesssim \mathrm{Pr}, \tag{2.21}$$

where use has been made of $\mathrm{Re}\sim v_{\rm pl}L\rho/\eta$. For $\mathrm{Pr}\gg 1$ there is a sizable range of $\mathrm{Ra}^{\rm corr}$ in which the Stokes approximation is justified. In passing, for $0<\mathrm{Ra}^{\rm corr}/\mathrm{Ra}_c-1\ll 1$, the theory of the amplitude equation [47] predicts

$$v_{\rm pl}L/D\sim(\delta T)_\perp/\Delta T\sim(\mathrm{Ra}^{\rm corr}/\mathrm{Ra}_c-1)^{1/2}, \tag{2.22}$$

from which we have $\mathrm{Nu}\text{-}1\sim\mathrm{Ra}^{\rm corr}/\mathrm{Ra}_c-1$ because the convective heat current is of order $C_p(\delta T)_\perp v_{\rm pl}$. In the following section we will estimate $v_{\rm pl}$ for a much larger Ra.

Analogously to Eq. (2.19), the inhomogeneous pressure deviation $p_{\rm inh}$ is estimated as $p_{\rm inh}\sim(\alpha_p\rho_c g/k)(\delta T)_\perp$. If we assume $p_1(t)\sim(\partial p/\partial T)_s\Delta T$ from Eq. (2.4) and $\Delta T\sim(\delta T)_\perp$ as in Eq. (2.20), we find that $p_{\rm inh}/p_1(t)$ is of order $\epsilon^{-\gamma}a_g/T_c k$ and is much smaller than 1 from Eq. (2.2). This estimation justifies the assumption of the homogeneity of $\delta p(\boldsymbol{r},t)+\rho_c g z$ made below in Eq. (2.4).

B. Free energy and heat production rate

In the presence of small deviations of the temperature and the density, δT and $\delta\rho$, around an reference equilibrium state, we have an increase of the free energy functional δF. Up to the bilinear order of the deviations, it is of the form [23,48],

$$\delta F=\int d\boldsymbol{r}\left[\frac{C_V}{2T}(\delta T)^2+\frac{1}{2\rho^2 K_T}(\delta\rho)^2+gz\,\delta\rho\right], \tag{2.23}$$

where the third term is the potential energy in gravity. All the deviations are assumed to change slowly in space compared with the thermal correlation length ξ. If we express $\delta\rho$ in terms of δT as in Eq. (2.14), we obtain

$$\delta F=\frac{1}{2T}\int d\boldsymbol{r}[C_p(\delta T-\langle\delta T\rangle)^2+C_V\langle\delta T\rangle^2], \tag{2.24}$$

where the constant term is omitted. We notice that δF decreases dramatically for $\gamma_s\gg 1$ in the process of adiabatic temperature homogenization. Furthermore, in the presence of velocity field, the total free energy change is the sum of δF and the kinetic energy of the velocity field,

$$F_K=\frac{1}{2}\int d\boldsymbol{r}\rho\boldsymbol{v}^2. \tag{2.25}$$

Its time derivative is calculated from our dynamic equations (2.7) and (2.17) in the form,

$$\frac{d}{dt}(\delta F+F_K)=-\int d\boldsymbol{r}(\epsilon_{\rm th}+\epsilon_{\rm vis}) +\lambda T^{-1}\int da[\,\delta T(\boldsymbol{n}\cdot\boldsymbol{\nabla}\delta T)], \tag{2.26}$$

where $\epsilon_{\rm th}$ and $\epsilon_{\rm vis}$ are the thermal and viscous heat production rates (per unit volume) [34], respectively, defined by

$$\epsilon_{\rm th}=\lambda T^{-1}|\boldsymbol{\nabla}\delta T|^2, \tag{2.27}$$

$$\epsilon_{\rm vis}=\eta\sum_{ij}(\partial v_i/\partial x_j)^2. \tag{2.28}$$

In the second term of Eq. (2.26) the surface integral is over the boundary of the cell, $\boldsymbol{n}$ being the outward unit vector. In terms of the heat flux from the bottom Q, it is expressed as $VQ\Delta T/TL$ if the top temperature is fixed.

C. Basic relations in steady states

We consider steady convective states in the Rayleigh-Bénard geometry, in which the flow pattern is either time-independent not far above the convection onset or chaotic at larger Ra. We treat ΔT as a constant parameter. Under the condition of fixed heat flux at the bottom, however, $\Delta T(t)$ exhibits rapidly varying fluctuations in chaotic states. In this case ΔT in the following relations represents the time-average of $\Delta T(t)$. The steady state averages (over space and time) will be denoted by $\langle\cdots\rangle_s$ to distinguish them from the space averages $\langle\cdots\rangle$ used so far.

We make Eqs. (2.8) and (2.17) dimensionless by measuring space and time in units of L and L^2/D and setting $\tilde{\boldsymbol{r}}=L^{-1}\boldsymbol{r}$ and $\tilde{t}=DL^{-2}t$. The temperature deviation is written as

$$\delta T(\boldsymbol{r},t)/\Delta T=1-\tilde{z}+\mathrm{Ra}^{-1}\mathcal{F}(\tilde{\boldsymbol{r}},\tilde{t}), \tag{2.29}$$

where $\tilde{z}=z/L$. The dimensionless function $\mathcal{F}$ becomes nonvanishing in convective states and obeys

$$\left(\frac{\partial}{\partial\tilde{t}}+\boldsymbol{V}\cdot\tilde{\boldsymbol{\nabla}}-\tilde{\boldsymbol{\nabla}}^2\right)\mathcal{F}=\mathrm{Ra}^{\rm corr}V_z+\alpha_s\frac{d}{d\tilde{t}}\langle\mathcal{F}\rangle, \tag{2.30}$$

where $\tilde{\boldsymbol{\nabla}}=L\boldsymbol{\nabla}$ is the space derivative in units of L. Then the (average) heat flux at the bottom is written as $Q=(\lambda\Delta T/L)[1+\mathrm{Ra}^{-1}f_\lambda]$, where

$$f_\lambda=-\langle(\partial\mathcal{F}/\partial\tilde{z})_{\tilde{z}=0}\rangle_s. \tag{2.31}$$

The f_λ is a function of $\mathrm{Ra}^{\rm corr}$ and Pr. The Nusselt number $\mathrm{Nu}=QL/\lambda\Delta T$ is expressed as

$$\mathrm{Nu}=1+\mathrm{Ra}^{-1}f_\lambda . \tag{2.32}$$

As the boundary condition of $\mathcal{F}$ we require $\mathcal{F}=0$ at $\tilde{z}=0$ and 1 if T_{top} and T_{bot} are fixed. However, if T_{top} and Q at the bottom are fixed, we have $\mathcal{F}=0$ at $\tilde{z}=0$ and $\partial\mathcal{F}/\partial\tilde{z}=\mathrm{Ra}(\mathrm{Nu}-1)$ at $\tilde{z}=0$. The dimensionless velocity $\boldsymbol{V}(\tilde{\boldsymbol{r}},\tilde{t})=(L/D)\boldsymbol{v}$ obeys

$$\frac{1}{\mathrm{Pr}}\left(\frac{\partial}{\partial\tilde{t}}+\boldsymbol{V}\cdot\tilde{\boldsymbol{\nabla}}\right)\boldsymbol{V}=-\tilde{\boldsymbol{\nabla}}P_{\mathrm{inh}}+\mathcal{F}\boldsymbol{e}_z+\tilde{\boldsymbol{\nabla}}^2\boldsymbol{V}, \tag{2.33}$$

where P_{inh} ensures $\tilde{\boldsymbol{\nabla}}\cdot\boldsymbol{V}=0$.

Here we assume that the piston term, the second term on the right-hand side of Eq. (2.30), can be neglected in steady states. For $\epsilon=0.05$, the piston term in steady states is less than a few percents of the convection term $\boldsymbol{v}\cdot\tilde{\boldsymbol{\nabla}}\mathcal{F}$ in Eq. (2.30) except at the boundaries. It thus produces no significant effects on steady state heat transport (on Nu), while it can be crucial in the initial transient stage [31]. Then, if the piston term in Eq. (2.30) is neglected, Eqs. (2.30) and (2.33) become of the same form as those of usual incompressible fluids except that $\mathrm{Ra}^{\mathrm{corr}}$ appears in place of Ra. At much smaller ϵ, however, this assumption might be questionable, because the noise part of $\langle\mathcal{F}\rangle$ grows as $\epsilon\to0$, as will be discussed in the following section. We may conclude the following (at least for not very small ϵ). (i) It follows the Gitterman-Steinberg criterion $\mathrm{Ra}^{\mathrm{corr}}>\mathrm{Ra}_c$ in convective states in the compressible case [32,33]. (ii) It is more nontrivial that the combination

$$\mathrm{Ra(Nu\text{-}1)}=f_\lambda(\mathrm{Ra}^{\mathrm{corr}},\mathrm{Pr}) \tag{2.34}$$

should be a universal function of $\mathrm{Ra}^{\mathrm{corr}}$ and Pr from Eq. (2.32) in agreement with the experiments [12,16]. Notice that $\mathrm{Ra(Nu\text{-}1)}=f_\lambda(\mathrm{Ra,Pr})$ holds for incompressible fluids in terms of the same f_λ. These experiments and more decisively that by Ahlers and Xu [15] indicate that f_λ should be nearly independent of Pr once Pr considerably exceeds 1. In the 3D simulation by Verzicco and Camussi [41], Nu became independent of Pr for $\mathrm{Pr}\gtrsim0.5$. Theoretical support of this behavior using scaling arguments was presented in Ref. [7].

In steady states we may also derive some exact relations for variances among δT and $\boldsymbol{v}$. Using the dynamic equations (2.8) and (2.17) we calculate the averages of $\partial(\delta T)^2/\partial t$, $\partial v^2/\partial t$, and $\partial(z\,\delta T)/\partial t$ to obtain

$$\langle|\boldsymbol{\nabla}\,\delta T|^2\rangle_s=a_{\mathrm{th}}^2+a_{\mathrm{th}}(a_{\mathrm{th}}-a_g)(\mathrm{Nu}-1), \tag{2.35}$$

$$\sum_{ij}\langle(\partial v_i/\partial x_j)^2\rangle_s=\mathrm{Ra}(D/L^2)^2(\mathrm{Nu}-1). \tag{2.36}$$

We also obtain a cross correlation,

$$\langle v_z\delta T\rangle_s=a_{\mathrm{th}}D(\mathrm{Nu}-1), \tag{2.37}$$

which is nothing but the average convective heat flux (if λC_p is multiplied). Here $a_{\mathrm{th}}\equiv\Delta T/L=-\langle d\,\delta T/dz\rangle_s$ is the average temperature gradient and a_g is the adiabatic temperature gradient defined by Eq. (1.2). If we use the usual hydrodynamic equations for incompressible fluids, the right-hand side of Eq. (2.35) becomes $a_{\mathrm{th}}^2\mathrm{Nu}$, while Eqs. (2.36) and (2.37) remain the same [2]. In addition, Eq. (2.35) indicates $a_{\mathrm{th}}>a_g$ in convective states in which $\mathrm{Nu}>1$. This is consistent with the convection criterion $\mathrm{Ra}^{\mathrm{corr}}>\mathrm{Ra}_c$. We obtain the averages of the two dissipation rates in Eqs. (2.27) and (2.28) by multiplying λ/T and η to Eqs. (2.35) and (2.36), respectively. Using the thermodynamic identity $T\alpha_p=C_p(\partial T/\partial p)_s$, we obtain

$$\langle\epsilon_{\mathrm{th}}\rangle_s+\langle\epsilon_{\mathrm{vis}}\rangle_s=T^{-1}\lambda a_{\mathrm{th}}^2\,\mathrm{Nu}, \tag{2.38}$$

$$(\langle\epsilon_{\mathrm{th}}\rangle_s-T^{-1}\lambda a_{\mathrm{th}}^2)/\langle\epsilon_{\mathrm{vis}}\rangle_s=a_{\mathrm{th}}/a_g-1. \tag{2.39}$$

The first relation (2.38) also follows from the average of Eq. (2.26). The second relation (2.39) holds only in convective states ($\mathrm{Nu}>1$) where $\epsilon_{\mathrm{vis}}>0$. For the usual hydrodynamic equations of incompressible fluids the right-hand side of Eq. (2.39) is replaced by $C_pa_{\mathrm{th}}/T\alpha_p\rho g=a_{\mathrm{th}}/a_g$.

III. SIMULATION RESULTS

We perform numerical analysis of Eqs. (2.8) and (2.17) in 2D using parameters of ^{3}He in a cell with $L=1.06$ mm. The reduced temperature is $\epsilon=0.05$ (except in Fig. 11), where $\gamma_s=22.8$, $T\alpha_p=26.9$, $\lambda=1.88\times10^{-4}$ ergs/(cm^2 s K), $D=5.42\times10^{-5}$ cm^2/s, and $\mathrm{Pr}=7.4$ [16,17,31]. The condition (2.2) is well satisfied. The piston time t_1 in Eq. (2.15) is given by 0.42 s. We apply a constant heat flux Q at the bottom $z=0$ for $t>0$ with a fixed top temperature T_{top} at $z=L$. In steady states we have $\mathrm{Ra}^{\mathrm{corr}}/\mathrm{Ra}_c=0.90[\Delta T/a_gL-1]$, where $a_gL=3.57$ μK. Thus $(\Delta T)_{\mathrm{on}}=7.6$ μK and $Q_{\mathrm{on}}=13.5$ nW/s at the convection onset. We assume homogeneity of the boundary temperatures, T_{top} and T_{bot}, in the lateral x direction.

In the experiments the aspect ratio was 57, so in the simulation [31] the periodic boundary condition was imposed in the x direction with period $4L$. This period was chosen because the roll period is close to $2L$ slightly above the onset for infinite lateral dimension [1]. Then, in steady states in the region $1<Q/Q_{\mathrm{on}}\lesssim5$, the linear relation

$$Q/Q_{\mathrm{on}}-1\cong A_0[\Delta T/(\Delta T)_{\mathrm{on}}-1] \tag{3.1}$$

was numerically obtained with $A_0\cong2.2$ in good agreement with the experiments. From $\mathrm{Nu}=[Q/\Delta T]/[Q_{\mathrm{on}}/(\Delta T)_{\mathrm{on}}]$, the behavior of Nu is known from Eq. (3.1) in the range $1<Q/Q_{\mathrm{on}}\lesssim5$. In particular, slightly above the onset, we have

$$\mathrm{Nu}-1\cong A_1(\mathrm{Ra}^{\mathrm{corr}}/\mathrm{Ra}_c-1)+\cdots, \tag{3.2}$$

where $A_1\cong0.64$ in fair agreement with the theoretical value ($A_1\cong0.70$ for $\mathrm{Pr}=7.4$) [49]. This behavior is also consistent with Eq. (2.22).

In this work we are interested in fluid motion for relatively large Ra up to 3×10^6. In the following we show two sets of the numerical results. In the first set, periodic sidewalls are assumed at $x=0$ and $x=L_\perp$ with period $L_\perp=4L$ as in Ref. [31]. In Table I the steady state values of ΔT, $\mathrm{Ra}^{\mathrm{corr}}$, Ra, Nu, and $\overline{\mathrm{Re}}$ are written, where $\overline{\mathrm{Re}}$ is a Reynolds number

TABLE I. Parameters at $\epsilon=0.05$ in steady states for periodic sidewalls.

$Q(\mu$W/cm s)	ΔT (mK)	$\mathrm{Ra}^{\mathrm{corr}}$	Ra	Nu-1	$\overline{\mathrm{Re}}$
0.0458	0.0154	3.43×10^3	6.69×10^3	0.714	0.655
0.965	0.135	5.71×10^4	5.87×10^4	3.04	3.035
122.2	6.89	2.91×10^6	2.91×10^6	9.29	7.89

to be defined in Eq. (3.11). They are obtained for $Q=0.0458$ μW/cm^2 ($\cong 3.4Q_{\mathrm{on}}$), 0.965 μW/cm^2 ($\cong 71Q_{\mathrm{on}}$), and 122.2 μW/cm^2($\cong 9\times10^3Q_{\mathrm{on}}$). For the smallest Q the system tends to a time-independent convective state, as already studied in Ref. [31], while for the other values of Q the system tends to a chaotic state without macroscopic boundary shear flow. In the second set, we perform simulations for $A=1$, 2, and 3 with insulating and rigid sidewalls at $x=0$ and AL, at which $\boldsymbol{v}=0$ and through which there is no heat flux ($\partial\delta T/\partial x=0$), as will be presented in Figs. 4, 12, and 13.

In addition, if the temperature difference will be simply written as ΔT, it should be taken as the time average of $\Delta T(t)$ in a steady state. We also assume that Pr is considerably larger than 1 in the following arguments.

A. Transient behavior

We show numerically calculated $\Delta T(t)=T_{\mathrm{bot}}(t)-T_{\mathrm{top}}$ for $Q=0.965$ μW/cm^2 in Fig. 1(a) and for $Q=122.2$ μW/cm^2 in Fig. 1(b). They nearly coincide with the upper broken curve without convection ($\boldsymbol{v}=\mathbf{0}$) in the initial stage before the maximum is attained. The latter curve is calculated from Eq. (2.8) as

$$[\Delta T(t)]_0=\frac{Q}{\lambda}\sqrt{\frac{Dt}{\pi}}\left[4-\int_0^\infty\frac{ds}{\sqrt{\pi s}}\cdot\frac{1-e^{-s}}{s+t/t_1}\right], \tag{3.3}$$

where t_1 is defined by Eq. (2.15) and the integral in the brackets behaves as $(\pi t_1/t)^{1/2}$ for $t\gg t_1$ [23]. If the piston term is absent and $\boldsymbol{v}=\mathbf{0}$, Eq. (2.8) becomes the simple diffusion equation, yielding $[\Delta T(t)]_0=(2Q/\lambda)(Dt/\pi)^{1/2}$, which is about half of $[\Delta T(t)]_0$ in Eq. (3.3) for $t\gg t_1$ (see Fig. 3 in Ref. [31]). We also show the numerically calculated $\Delta T(t)$ at fixed pressure where the piston term is absent [$\alpha_s=0$ in Eq. (2.8)] but $\boldsymbol{v}\neq\mathbf{0}$. In (a) the experimental curve is shown to have a lower peak and overdamp more slowly than in our simulation. In (b) the selected value of Q is in the region where no overshoot was observed in the experiment. See also Fig. 11, where the numerical curves of $\Delta T(t)$ will be given for other choices of the parameters.

In Fig. 2 we show time evolution of the temperature profile at $Q=122.2$ μW/cm for periodic sidewalls. In A and B small-scale mushroomlike plumes are ejected from the bottom. In C and D they reach the top and are flattened there. In this initial stage the typical raising speed v_{pl} is estimated as L/t_{tr} where t_{tr} is the traversing time. From A–C we find that it is nearly equal to the free-fall velocity v_g defined by

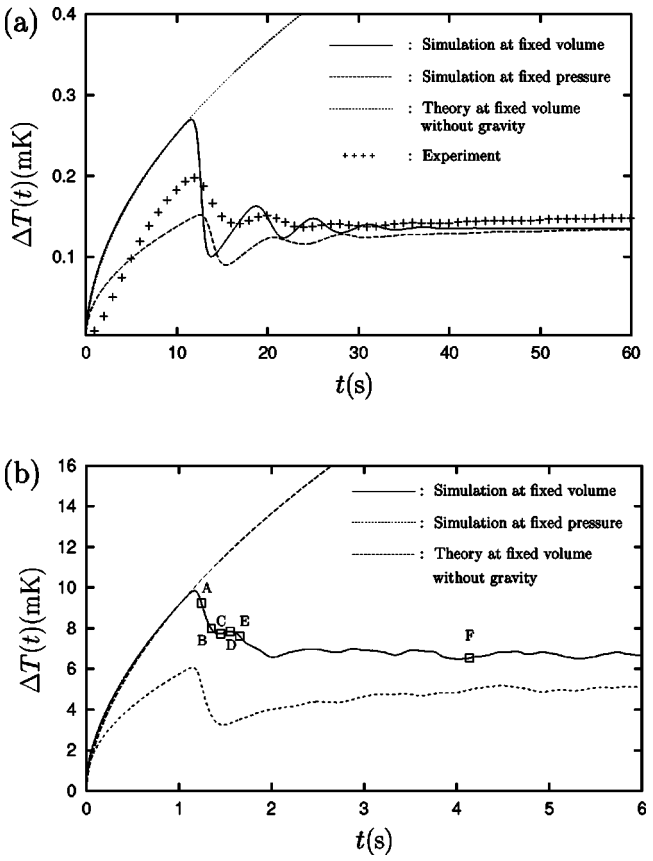

FIG. 1. $\Delta T(t)$ vs time (solid line) calculated from Eqs. (2.8) and (2.17) for (a) $Q=0.965$ μW/cm^2 and (b) $Q=122.2$ μW/cm^2. The temperature profiles for the points (□) on the curve in (b) are given in Fig. 2. The experimental data (+) [17] are shown in (b). The upper broken curves in (a) and (b) represent the theoretical result (3.3) obtained from integration of Eq. (2.8) with $\boldsymbol{v}=\mathbf{0}$. The dotted curves represent the numerical ones in the fixed pressure condition without the piston effect.

$$v_g=(Lg\alpha_p\Delta T)^{1/2}=(\mathrm{Ra\ Pr})^{1/2}D/L, \tag{3.4}$$

which is 2.37 cm/s. In this case the plumes leave the bottom at zero velocity and go upward with their velocity roughly of the form,

$$v_{\mathrm{pl}}(t)=v_\infty\{1-\exp[-(t-t_0)/t_{\mathrm{vis}}]\}, \tag{3.5}$$

where t_0 is the departure time, $t_{\mathrm{vis}}\sim\rho R^2/\eta$ is the viscous relaxation time with R being the plume size, and

$$v_\infty\sim R^2g\rho\alpha_p\Delta T/\eta \tag{3.6}$$

is the terminal velocity achieved by balance between the buoyancy and the viscous drag. For $t_{\mathrm{tr}}\ll t_{\mathrm{vis}}$ the viscous drag is negligible and we have $v_{\mathrm{pl}}(t)\sim v_g^2(t-t_0)/L$ and $t_{\mathrm{tr}}\sim L/v_g$. Thus, if the initial velocity is much less than v_g, the *free-fall* condition becomes

$$R/L\gg(\mathrm{Pr/Ra})^{1/4}, \tag{3.7}$$

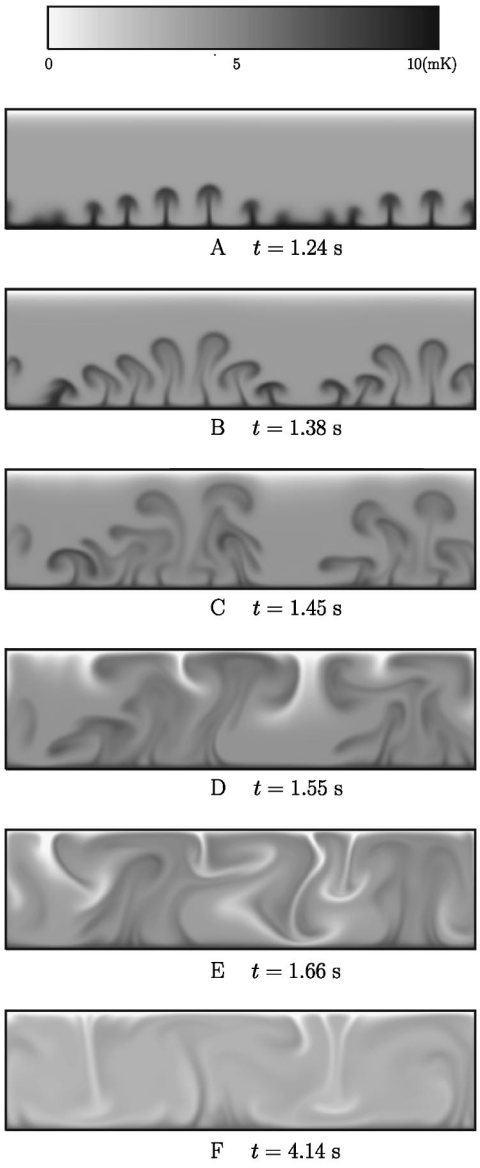

FIG. 2. Temperature profiles at *A*, *B*, *C*, *D*, *E*, and *F* on the curve of $Q = 122.2\ \mu\mathrm{W/cm^2}$ in Fig. 1(b) (□). The temperature (and velocity) deviations are more enhanced in the transient states *A*–*E* than in a steady state *F*. The δT at the bottom boundary $z = 0$ is equal to $\Delta T(t)$ in Fig. 1(b). The plumes tend to be connected between bottom and top because Pr = 7.4.

under which $v_\infty = (R/L)^2(\mathrm{Ra/Pr})^{1/2} v_g \gg v_g$. In Fig. 2, $R/L \sim 1/3$ and $(\mathrm{Pr/Ra})^{1/4} \sim 0.04$, so the above condition is satisfied.

With the arrival of the plumes the heat current increases at the top, because T_{top} is fixed, and a negative deviation of δs is produced in a layer near the top. As can be known from Eq. (2.13), the piston effect is then operative, resulting in a homogeneous lowering of the temperature in the whole cell. In the time region around *E* the fluid is vigorously mixed with high Reynolds numbers. More precisely, the height-dependent Reynolds number $\mathrm{Re}(z,t)$ to be defined in Eq. (3.12) below is about 20 except in the vicinity of the boundaries. A downward flow of cooler fluid regions is then produced from the top. In the steady state *F*, the temperature deviation becomes considerably smaller than in the transient states, and the localized boundary shear flows are produced between outgoing and incoming plumes with thickness ℓ_v much smaller than *L*.

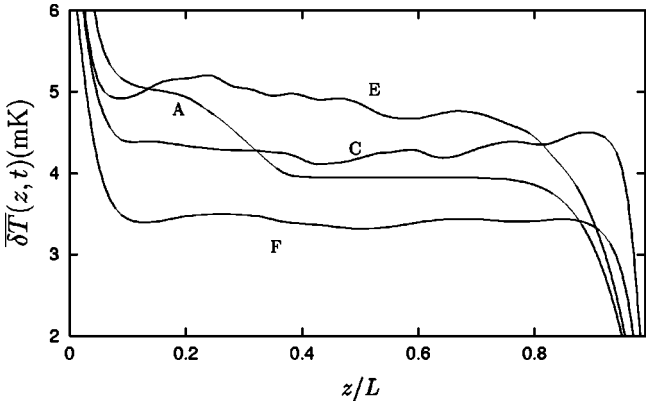

FIG. 3. Time evolution of $\overline{\delta T}(z,t)$ defined by Eq. (3.5) at the points *A*, *C*, *E*, and *F* in Fig. 1(b) for $Q = 122.2\ \mu\mathrm{W/cm^2}$.

The overshoot is more clearly illustrated in Fig. 3, which displays the average of $\delta T(x,z,t)$ taken in the *x* direction,

$$\overline{\delta T}(z,t) \equiv \int_0^{L_\perp} \frac{dx}{L_\perp} \delta T(x,z,t), \tag{3.8}$$

for the points *A*, *C*, *E*, and *F* in Fig. 1(b). As a characteristic feature, the temperature in the interior consists of global changes due to the piston effect and bumps due to localized plumes. In *E* the cooler layer becomes thicker temporarily near the top due to the excess heat flow.

In our simulation the raising plumes leave the bottom and reach the top nearly simultaneously, resulting in a homogeneous temperature change.

(i) Not far above the onset this mechanism is the main cause of the overshoot in compressible fluids. Note that a small peak appears in $\Delta T(t)$ even in the fixed pressure case ($\gamma_s = 1$) as shown in Fig. 2 of Ref. [31] and as was observed by Behringer and Ahlers [50]. Furthermore, in Ref. [31], the time scale of the overshoot [from the maximum to the minimum of $\Delta T(t)$] due to the piston effect was predicted to be of order $t_D/(\mathrm{Ra}^{\mathrm{corr}}/\mathrm{Ra}_c - 1)$, where $t_D = L^2/4D (\cong 50\ \mathrm{s})$ is the diffusion time. This fairly agrees with later analysis of the experimental data [51].

(ii) For much larger *Q* such as those in Figs. 1(a) and 1(b), however, the downward flow from the top is also rapid enough to produce large overshoot, as demonstrated by the curves at fixed (height-dependent) pressure. Whether fixed is the volume or the pressure, the time scale of the overshoot is of the order of the traversing time L/v_g of the plumes due to gravity.

As regards the overshoot behavior of $\Delta T(t)$, agreement between our simulation and the experiment [17] becomes worse with increasing *Q*. We point out the possibility that in the experiment a synchronous arrival of plumes at the top might have not been realized for very large *Q* or for very short L/v_g because of large lateral dimensions of the cell

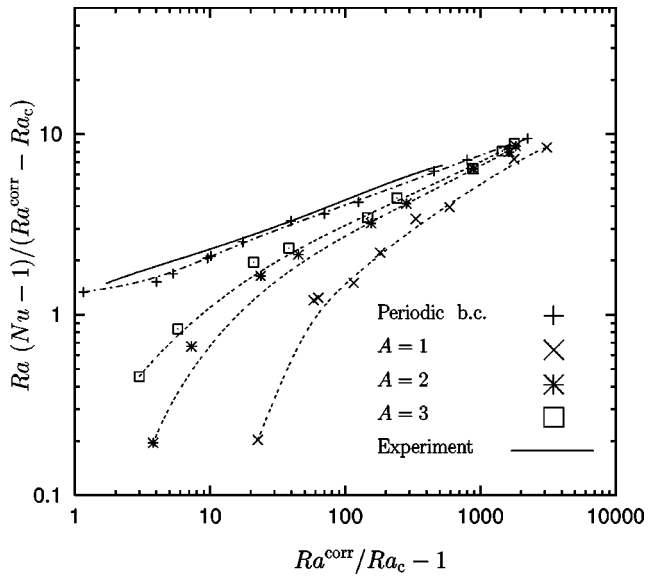

FIG. 4. Numerical results of Ra $(\mathrm{Nu}-1)/(\mathrm{Ra}^{\mathrm{corr}}-\mathrm{Ra}_c)$ vs $\mathrm{Ra}^{\mathrm{corr}}/\mathrm{Ra}_c-1$ in steady states, obtained under the periodic boundary condition (+) and for $A=3$ (□), 2 (*), and 1 (×). The first curve (+) is close to the experimental results for $A=57$ [17] (solid line) and is well fitted to the scaling form (1.5) with $a\cong 2/7$ for $\mathrm{Ra}^{\mathrm{corr}}/\mathrm{Ra}_c \gtrsim 10$. With the aspect ratio A decreasing, crossover to the scaling occurs at much larger $\mathrm{Ra}^{\mathrm{corr}}$.

used. That is, if some plumes arrive at the top and others leave the bottom at the same time, negative interference between currents up and down will suppress overshoot.

B. Steady-state behavior

Now we discuss the Nusselt number Nu in steady states. Figure 4 shows the combination $\mathrm{Ra(Nu\text{-}1)}/(\mathrm{Ra}^{\mathrm{corr}}-\mathrm{Ra}_c)$ vs $\mathrm{Ra}^{\mathrm{corr}}/\mathrm{Ra}_c-1$ for periodic sidewalls and for $A=1$, 2, and 3. This combination depends on $\mathrm{Ra}^{\mathrm{corr}}$ and A from Eq. (2.34) in steady states. The data (solid line) [17] excellently agree with the numerical results for periodic sidewalls. We find that the scaling relation (1.5) nicely holds for $\mathrm{Ra}^{\mathrm{corr}}/\mathrm{Ra}_c \gtrsim 10$ for periodic sidewalls, while it holds only for $\mathrm{Ra}^{\mathrm{corr}}/\mathrm{Ra}_c \gtrsim 10^3$ at $A=1$. The exponent a in Eq. (1.5) is close to 2/7, but $a=1/4$ is also consistent with our numerical data. If $A\sim 1$ and $\mathrm{Ra}^{\mathrm{corr}}$ is not very large such that the plume size is of order L, large-scale fluid motions are suppressed by the rigid sidewalls. This marked tendency of the A-dependent crossover of Nu was already reported in measurements for $A=0.5$, 1, and 6.7 [10].

In Fig. 5 we show the steady-state temperature deviation $\overline{\delta T}(z)$ averaged in the x direction as in Eq. (3.8) and in time for the three values of Q in Table I for periodic sidewalls with period $L_\perp = 4L$. The averages taken along the x direction become only weakly fluctuating in time in steady chaotic states (the relative fluctuations being of order 10% for the largest Q). As has been observed ubiquitously in the previous simulations, the temperature gradient becomes localized within thermal boundary layers with thickness ℓ_T. Because $\Delta T \cong 2\ell_T Q/\lambda$ for $\ell_T \ll L$, it is related to Nu by Eq. (1.6). The arrows in Fig. 5 represent the maximum points,

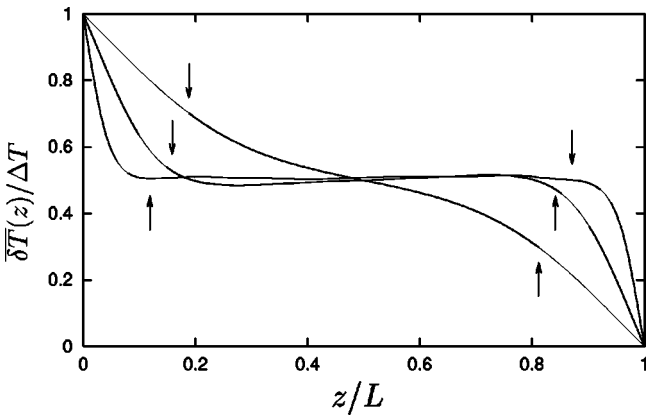

FIG. 5. Height-dependent average temperature profiles $\overline{\delta T}(z)$ divided by ΔT in steady states for the three Q values in Table I. The arrows represent the maxima of $v_x^*(z)$ in Fig. 6(a).

$z=\ell_v$ and $L-\ell_v$, of the variance of the horizontal velocity defined by

$$v_x^*(z)=\left[\int_0^{L_\perp}\frac{dx}{L_\perp}v_x(x,z,t)^2\right]^{1/2}. \tag{3.9}$$

In Fig. 6 we plot the normalized velocity variances, $v_x^*(z)/v_g$ in (a) and $v_z^*(z)/v_g$ in (b), where v_g is defined by Eq. (3.4) and

$$v_z^*(z)=\left[\int_0^{L_\perp}\frac{dx}{L_\perp}v_z(x,z,t)^2\right]^{1/2}. \tag{3.10}$$

The time average of v_x^2 and v_z^2 in the brackets is also taken in these figures. On one hand, v_x^* take maxima at $z=\ell_v$ and $L-\ell_v$, where ℓ_v is hardly distinguishable from ℓ_T. On the other hand, v_z^* is largest at the middle of the cell. We also find that the sum (the kinetic-energy variance) $(v_x^*)^2+(v_z^*)^2$ is nearly constant in the interior, which was a finding reported in Ref. [42]. At large Ra the maxima of v_x^* and v_z^* are of the same order and will be identified as the typical plume velocity v_{pl}. In our simulation we have $v_{\mathrm{pl}}\sim 0.1 v_g$ $(\propto \mathrm{Ra}^{1/2})$, which is consistent with velocity measurements [9,22].

Kerr and Herring [43] made similar plots of the height-dependent velocity variances in their 3D simulations for free-slip sidewalls. They found that the characteristic length ℓ_v defined by the peak positions of $v_x^*(z)$ becomes longer than $\ell_T = L/2\,\mathrm{Nu}$ with increasing Ra; for example, for $\mathrm{Pr}=7$ they obtained $\ell_v/\ell_T \sim 1$ at $\mathrm{Ra}=10^4$ and $\ell_v/\ell_T \sim 3$ at $\mathrm{Ra}=10^7$. Verzicco and Camussi obtained a similar slow growing of ℓ_v/ℓ_T at large Ra for $\mathrm{Pr}>1$ in their 3D simulation with $A=1$ [41]. Also similarly, our 2D simulation with $\mathrm{Pr}=7.4$ gives $\ell_v/\ell_T=2.54$ and 1.1 for $Q=122.2$ and 0.965 μW/cm, respectively, but we cannot draw a definite conclusion because of our limited range of Ra.

In Fig. 7 we plot an overall Reynolds number $\overline{\mathrm{Re}}$ vs $\mathrm{Ra}^{\mathrm{corr}}/\mathrm{Ra}_c-1$ in the simulation for periodic sidewalls. It is defined by

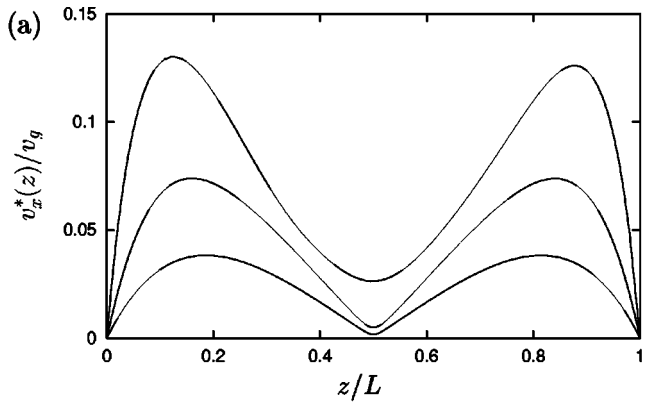

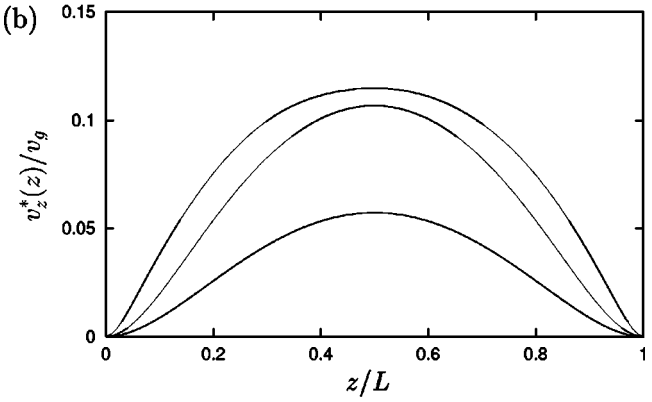

FIG. 6. Normalized height-dependent variances, $v_x^*(z)/v_g$ for the horizontal velocity in (a) and $v_z^*(z)/v_g$ for the vertical velocity in (b) in steady states for the three Q values in Table I.

$$\overline{\mathrm{Re}}=\frac{\rho}{\eta}[\langle|\boldsymbol{v}\cdot\boldsymbol{\nabla}\boldsymbol{v}|^2\rangle/\langle|\boldsymbol{\nabla}^2\boldsymbol{v}|^2\rangle]^{1/2}, \tag{3.11}$$

where the averages are taken in the whole space region. The $\overline{\mathrm{Re}}$ is smaller than 1 for $R^{\mathrm{corr}}/R_c \lesssim 5$ [31]. For larger values of R^{corr}, it exceeds 1 and the effective exponent $\partial(\ln\overline{\mathrm{Re}})/\partial(\ln \mathrm{Ra}^{\mathrm{corr}})$ is from 1/4 to 1/3. However, as suggested by Fig. 6, the strength of the velocity fluctuations strongly depends on the distance from the boundary, so it is more informative to introduce a height-dependent Reynolds number,

$$\overline{\mathrm{Re}}(z)=\frac{\rho}{\eta}\left[\int_0^{L_\perp}dx|\boldsymbol{v}\cdot\boldsymbol{\nabla}\boldsymbol{v}|^2/\int_0^{L_\perp}dx|\boldsymbol{\nabla}^2\boldsymbol{v}|^2\right]^{1/2}, \tag{3.12}$$

where the time averages of the integrands are taken. As shown in Fig. 8, $\hat{\mathrm{Re}}(z)$ takes maxima at $z\sim\ell_v$ and $L-\ell_v$ of order

$$\hat{\mathrm{Re}}(\ell_v)\sim\ell_v v_{\mathrm{pl}}\rho/\eta, \tag{3.13}$$

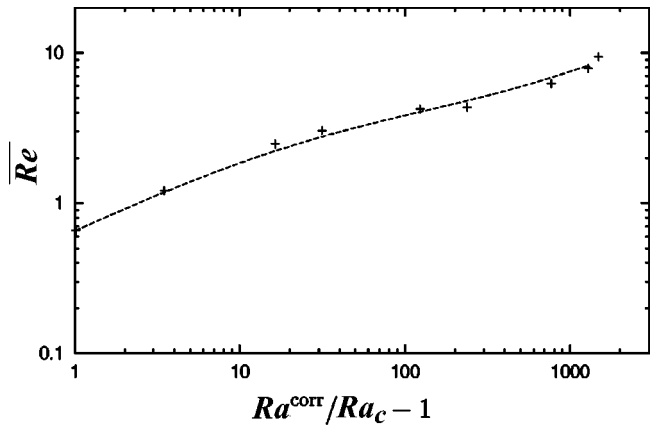

FIG. 7. Oveall Reynolds number $\overline{\mathrm{Re}}$ defined by Eq. (3.11) as a function of $\mathrm{Ra}^{\mathrm{corr}}/\mathrm{Ra}_c-1$ in steady states for $Q=122.2$ μW/cm^2.

where $v_{\mathrm{pl}}\sim v_x^*(\ell_v)$. This relation indicates $\hat{\mathrm{Re}}(\ell_v)\sim\mathrm{Ra}^{1/2-a}$ with $a\cong 2/7$ from $v_{\mathrm{pl}}\sim 0.1 v_g$ and $\ell_v\sim\ell_T$. The $\hat{\mathrm{Re}}(z)$ becomes considerably smaller in the interior than at $z\sim\ell_v$, whose origin is the sparseness of the plumes in the interior [see Eq. (3.20) below]. We confirm that $\overline{\mathrm{Re}}$ is of the order of the space average $\int_0^L dz\hat{\mathrm{Re}}(z)/L$. In the literature [2–7], however, the (large-scale) Reynolds number has been identified as $\overline{\mathrm{Re}}=v_{\mathrm{pl}}L\rho/\eta$, which is much larger than $\hat{\mathrm{Re}}(\ell_v)$ in Eq. (3.13) by L/l_v. [For roll patterns, as was discussed following Eq. (2.21), we uniquely have $\mathrm{Re}=v_{\mathrm{pl}}L\rho/\eta$.]

At very large Ra the boundary layers should gradually crossover from a laminar state to a turbulent state except within thin viscous sublayers with thickness z_0 much shorter than l_v. In the inertial region $z_0\lesssim z\lesssim\ell_v$ of the boundary layer, it is natural to expect the logarithmic velocity profile [34],

$$v_x^*(z)=b_0^{-1}(\sigma_0/\rho)^{1/2}[\ln(z/z_0)+c_0], \tag{3.14}$$

where σ_0 is the amplitude of the shear stress at the boundary with b_0 and c_0 being dimensionless numbers of order 1. We may set $\sigma_0=\eta\lim_{z\to 0}D_{xz}(z)$, where $D_{xz}(z)$ is the variance of the velocity gradient,

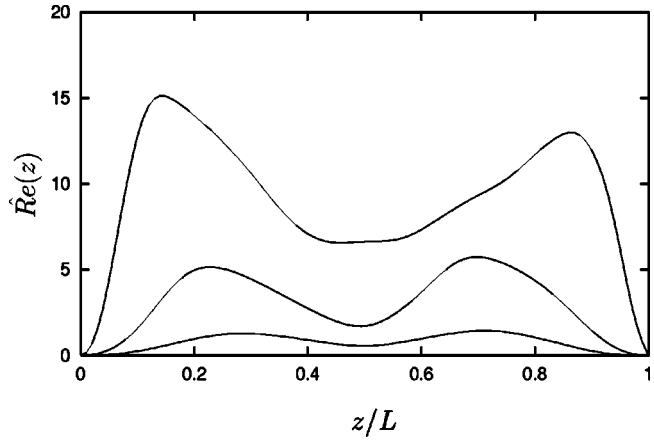

FIG. 8. Height-dependent Reynolds number $\hat{Re}(z)$ defined by Eq. (3.9) in steady states for the three Q values in Table I.

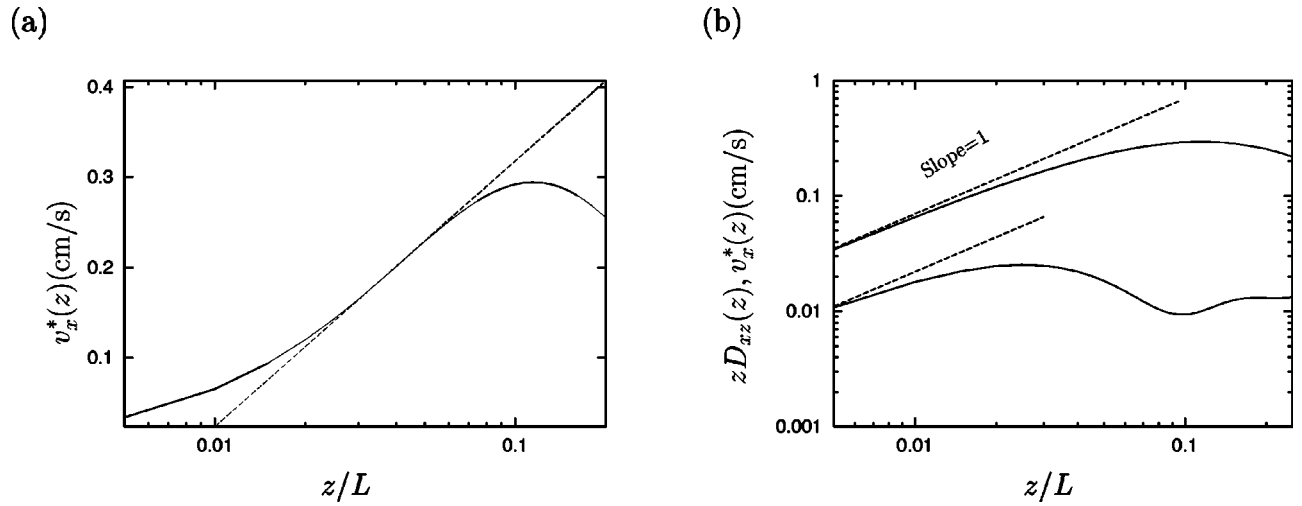

FIG. 9. (a) Height-dependent velocity variance $v_x^*(z)$ defined by Eq. (3.9) (solid line) on a semilogarithmic scale in steady states for $Q=122.2$ μW/cm^2. (b) $v_x^*(z)$ (upper curve) and velocity gradient variance $zD_{xz}(z)$ defined by Eq. (3.15) (lower curve) on a logarithmic scale.

$$D_{xz}(z)=\left[\int_0^{L_\perp}\frac{dx}{L_\perp}\left(\frac{\partial}{\partial z}v_x(x,z,t)\right)^2\right]^{1/2}. \tag{3.15}$$

Then $v_x^*(z)\cong(\sigma_0/\eta)z$ as $z\to 0$. It is appropriate to define z_0 as [34]

$$z_0=\eta/(\rho\sigma_0)^{1/2}, \tag{3.16}$$

which ensures $\hat{R}e(z_0)\sim 1$. The size of σ_0 should be equal to the typical size of $\rho v_x v_z$ at $z=\ell_v$ even if we consider localized shear flows for periodic sidewalls, so we also have

$$\sigma_0\sim\rho v_{\rm pl}^2. \tag{3.17}$$

The ratio of the two lengths z_0 and ℓ_v is given by

$$\ell_v/z_0\sim v_{\rm pl}\ell_v\rho/\eta\sim\hat{\rm Re}(\ell_v), \tag{3.18}$$

which grows with increasing Ra. In Fig. 9(a), $v_x^*(z)$ is fitted to the above logarithmic form in the inertial region for $Q=122.2$ μW/cm, where $(\sigma_0/\rho)^{1/2}=0.067v_g=0.16$ cm/s, $b_0=1.2$,$c_0=0.97$, and $z_0=0.025L$. In Fig. 9(b), we plot $v_x^*(z)$ and $zD_{xz}(z)$ on a logarithmic scale. We may conclude that these quantities do not behave as z in the inertial region of the boundary layers, although the present Ra is not large enough to unambiguously demonstrate the logarithmic velocity profile. Here we point out that our results are not consistent with Shraiman and Siggia's primary assumptions of $\ell_T<\ell_v$ and the linear profile of the mean shear flow, $v_x\propto z$, in the region $z<\ell_T$ [2,3].

In contrast to the averages taken along the x direction, those taken along the z direction are rapidly varying functions of time at large Ra due to the random plume motions. We consider the vertical velocity variance defined by

$$v_z^*(x,t)=\left[\int_0^L\frac{dz}{L}v_z(x,z,t)^2\right]^{1/2}. \tag{3.19}$$

In Fig. 10 we display snapshots of $v_z^*(x,t)$, where the time average is not taken and peaks arising from the plumes become more apparent with increasing Q. For our Ra realized, the space regions occupied by the plumes become more sparse with increasing Ra in the interior. As the plumes move through the cell, they remain distinguishable from the ambient fluid because the thermal diffusion length $(DL/v_{\rm pl})^{1/2}$ does not much exceeds ℓ_v. So we may define the volume fraction of the plumes $\phi_{\rm pl}$. The convective heat current is of order $\phi_{\rm pl}v_{\rm pl}C_p\Delta T\sim\lambda\,{\rm Nu}\,\Delta T/L$, leading to

$$\phi_{\rm pl}\sim D/\ell_T v_{\rm pl}, \tag{3.20}$$

which is of order $\Pr^{-1}\hat{\rm Re}(l_v)^{-1}\ll 1$ from Eq. (3.13). For much larger Ra, the plumes will generate smaller scale ed-

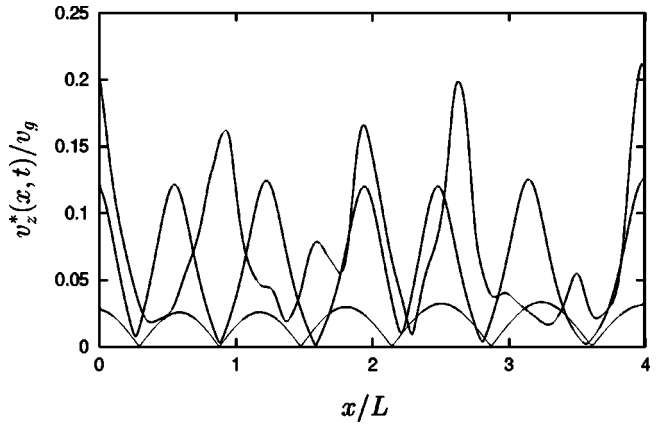

FIG. 10. Snapshots of the normalized velocity variance $v_z^*(x,t)/v_g$ averaged in the z direction defined by Eq. (3.19) for the three values of Q in Table I. The system is periodic with period $4L$ in the x direction. The peak heights increase with increasing Q. For the largest Q this quantity changes in time as the plumes move in the cell, while for the other Q it is weakly dependent on, or independent of, time.

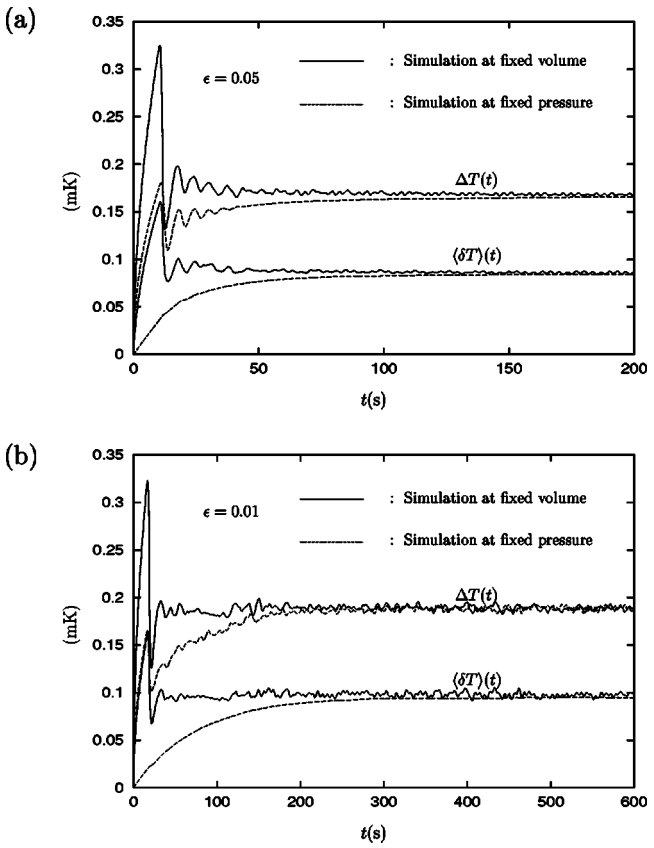

FIG. 11. $\langle \delta T \rangle(t)$ and $\Delta T(t)$ at fixed volume (solid line) and at fixed pressure (broken line) for $\epsilon = 0.05$ (upper figure) and 0.01 (lower figure). The noises of these quantities at fixed volume increase as the reduced temperature ϵ is decreased.

dies, ultimately leading to fully developed turbulence in the interior, as will be discussed in Sec. IV.

C. Overall temperature fluctuations

When a plume with a volume $V_{\rm pl}$ reaches the boundary, it transfers a heat of order $C_p \Delta T V_{\rm pl}$ to the boundary wall. As indicated by Eq. (2.13), the piston effect then gives rise to a homogeneous change in $\langle \delta T \rangle(t)$ of order

$$(\delta T)_{\rm pl} \sim \gamma_s (V_{\rm pl}/V) \Delta T. \tag{3.21}$$

Of course, the real plumes are extended objects and are continuously arriving at the boundary in high Ra convection. Thus $V_{\rm pl}/V$ in the above formula should be regarded as the fluctuation amplitude of the plume volume fraction $\phi_{\rm pl}$ in the interior, although we do not know about its dependence on Ra, etc., at present. If $T_{\rm top}$ and Q at the bottom are fixed as in our simulation, $\Delta T(t)$ should also consist of fluctuations of the same origin. Because of the strong critical divergence of γ_s, we expect that the relative noise amplitude $(\delta T)_{\rm pl}/\Delta T$ would increase as ϵ is decreased with a fixed size of ΔT.

Figure 11 displays time sequences of $\langle \delta T \rangle(t)$ and $\Delta T(t)$ at fixed volume and pressure for periodic sidewalls with $L_\perp = 4L$, which demonstrates strong correlations between these two deviations at fixed volume. Here we write the time average of $\Delta T(t)$ as $\overline{\Delta T}$ to avoid confusion. In Fig. 11(a) (upper figure) we set $\epsilon = 0.05$ ($\gamma_s = 22.8$), $\overline{\Delta T} = 0.17$ mK, Pr = 7.4, Ra $= 7.38 \times 10^4$, and Nu = 4.06, while in Fig. 11(b) (lower figure) we set $\epsilon = 0.01$ ($\gamma_s = 119$), $\overline{\Delta T} = 0.19$ mK, Pr = 37.7, Ra $= 4.14 \times 10^5$, and Nu = 6.04. The time average $\overline{\Delta T}$ is chosen to be only slightly different in the two cases. At fixed volume, the fluctuations of $\langle \delta T \rangle(t)$ and $\Delta T(t)$ are strongly correlated, and are larger and slower for Fig. 11(b) than for Fig. 11(a) in steady states ($t \gtrsim 100$). The normalized variance of $\Delta T(t)$, the square root of the time average of $[\Delta T(t)/\overline{\Delta T} - 1]^2$, is equal to 0.0069 for Fig. 11(a) and 0.012 for Fig. 11(b) at fixed volume. At fixed pressure, where the piston effect is absent, $\Delta T(t)$ exhibits noises much smaller than those at fixed volume and $\langle \delta T \rangle(t)$ smoothly changes in time. It is worth noting that this noise increase at fixed volume accompanied by an increase of Ra is contrary to the usually measured noise behavior of the temperature. For noncritical fluids, if the temperature is measured at the center of a cell, its fluctuation amplitude divided by ΔT is known to decrease with increasing Ra as $\mathrm{Ra}^{-\beta_n}$. The exponent β_n was about 0.15 in a cell with $A = 1$ [5,18].

D. Random reversal of macroscopic flow

For a convection cell with $A \sim 1$, it is well known that large-scale shear flow develops near the boundary of the cell for large enough Ra [19,21,22]. Moreover, it has also been observed that the global circulation changes its orientation over long time scales [21,19]. For the case of $A = 1$, $L = 1.06$ mm, $\epsilon = 0.05$, $Q = 40.7$ μW/cm^2, Ra $= 1.68 \times 10^6$ ($\cong \mathrm{Ra}^{\rm corr}$), Nu = 5.97, we plot a numerical time sequence of a circulation $\Gamma(t)$ in Fig. 12. Here

$$\Gamma(t) = \int_d^{L-d} dx [v_x(x, L-d, t) - v_x(x, d, t)]/L + \int_d^{L-d} dz [v_z(L-d, z, t) - v_z(d, z, t)]/L, \tag{3.22}$$

where the integration is along a square contour with distance $d = 0.05L$ from the cell boundary. This quantity is positive for clockwise circulation and negative for counterclockwise circulation. In Fig. 12, $\Delta T(t)$ is also plotted, which exhibits particularly large fluctuations on the occasion of orientation changes. This is a natural result because large-scale reorganization of the flow pattern is needed for an orientation change.

Figure 13 illustrates the velocity patterns at $t = 228$, 269, and 311 s in Fig. 12. They closely resemble a picture of the measured velocity pattern in Ref. [22]. Here the typical velocities of the macroscopic flow and the plumes are both of order 0.2 cm/s in agreement with the estimation (4.2). The circulation time ($\sim 4L/v_{\rm pl}$) is of order 2 s and is much shorter than the average period of the global orientation reversal (~ 50 s). At any times a small number of plumes with irregular shapes are emerging from the bottom, top, and side boundaries. In most times a large primary eddy is dominant

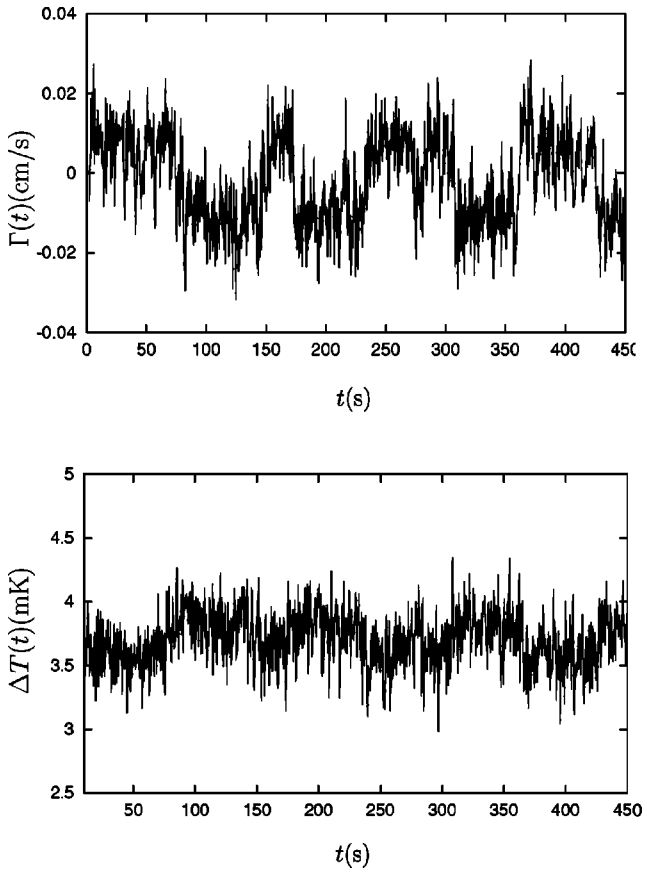

FIG. 12. Time evolution of the circulation $\Gamma(t)$ defined by Eq. (3.22) (upper figure) and $\Delta T(t)$ (lower figure) for $Q=122.2\ \mu\mathrm{W/cm^2}$ in a cell with $A=1$. The orientation of the macroscopic flow changes on a time scale of 50 s. The sign of $\Gamma(t)$ represents the orientation of the macroscopic circulation, while the fluctuations of $\Delta T(t)$ become large when the orientation changes.

in the middle region in coexistence with small counter-oriented eddies near the corners. However, when a plume moving through the cell is strong enough, it can suppress the preexisting primary eddy and cause a global orientation change.

IV. SCALING THEORY

Rayleigh numbers realized in the existing simulations are still moderate in the sense that the plumes do not have enough kinetic energies such that they do not generate fully developed turbulence in the interior. In this *preasymptotic* regime of steady states, we may understand the numerical and experimental data using a very simple *zeroth-order* theory. First, we set $\ell=\ell_T=\ell_v$ neglecting the possible small difference between ℓ_T and ℓ_v mentioned following Eq. (3.10). The plume sizes in the horizontal direction are also of order ℓ. Second, in our simulation the plumes are ejected into the interior with a velocity v_{pl}, for which the viscous drag and the buoyancy are balanced or

$$\eta l^{-2} v_{\mathrm{pl}} \sim \rho g \alpha_p \Delta T. \tag{4.1}$$

Thus v_{pl} is of the order of the terminal velocity $v_\infty \sim \mathrm{Ra}\, D l^2/L^3$ in Eq. (3.6) with $R\sim\ell$. In the interior we find that (i) gravity-induced acceleration of the plumes is suppressed by the viscous drag, (ii) $(v_x^*)^2+(v_z^*)^2$ is nearly independent of z as stated below Eq. (3.10), and (iii) the last two terms on the left-hand side of Eq. (2.17) are numerically of the same order. For example, the ratio of the average of $(\alpha_p g\,\delta T)^2$ in the x direction to that of $|(\eta/\rho)\boldsymbol{\nabla}^2\boldsymbol{v}|^2$ is about 4 at $z\sim l$ and is fluctuating around 1 in the interior for the largest Q in Table I. These support $v_{\mathrm{pl}}\sim v_\infty$ in the interior. Third, to the sum rule (2.36) for the velocity gradients, the contribution from the boundary layers is of order $v_{\mathrm{pl}}^2/\ell L$, while that from the interior is of order $\phi_{\mathrm{pl}} v_{\mathrm{pl}}^2/\ell^2 \sim D v_{\mathrm{pl}}/\ell^3$ from Eq. (3.20). If use is made of Eq. (4.1) and the sum rule (2.36), these boundary-layer and bulk contributions both become of order $\mathrm{Ra}\,\mathrm{Nu}(D/L^2)^2$, which has also been confirmed numerically. Thus,

$$v_{\mathrm{pl}} \sim \mathrm{Ra}^{1/2} D/L, \tag{4.2}$$

$$\mathrm{Nu} \sim L/\ell \sim 1/\phi_{\mathrm{pl}} \sim \mathrm{Ra}^{1/4}. \tag{4.3}$$

These quantities are independent of Pr. In particular, the independence of Nu on Pr is consistent with the experiments [13,15,17]. In accord with Eqs. (3.4) and (4.2), our data of the velocity ratio v_{pl}/v_g can well be fitted to $0.26\ \mathrm{Pr}^{-1/2}$ for Pr=7.4, 37.7, and 74.8 or for $\epsilon=0.05$, 0.01, and 0.005, respectively, at high Ra. In his 3D simulation [42] Kerr calculated the typical horizontal velocity v_{pl} at $z=\ell_v$ (u_w in his notation) and obtained $v_{\mathrm{pl}}/v_g=0.24$ for Pr=0.7.

Our height-dependent Reynolds number at $z=\ell$ in Eq. (3.13) becomes

$$\hat{\mathrm{Re}}(l) \sim \mathrm{Ra}^{1/4}/\mathrm{Pr}. \tag{4.4}$$

The usual large-scale Reynolds number is given by $\mathrm{Re}\sim v_{\mathrm{pl}} L\rho/\eta \sim \mathrm{Ra}^{1/2}/\mathrm{Pr}$. As $\hat{\mathrm{Re}}(l)$ exceeds a crossover value Re*, plumes will induce turbulence in the interior. Our simple scaling theory is valid for $\mathrm{Ra} \lesssim (\mathrm{Re}^*\mathrm{Pr})^4$. In our simulation we have $\hat{\mathrm{Re}}(l)\cong 0.38\,\mathrm{Ra}^{1/4}$, for Pr=7.4 or for $\epsilon=0.05$ so that if we set $\mathrm{Re}^*\sim 10^3$ (regarding plumes as jets [34]), the upper bound is crudely estimated as 5×10^{13}. The transition from the scaling [Eq. (4.3)] to the asymptotic scaling occurs over a very wide range of Ra. the sparseness of the plumes indicated by Eqs. (3.20) and (4.3) should also serve to decelerate the changeover into the asymptotic turbulent regime. Similarly, Grossmann and Lohse [6] considered a transition of a laminar boundary-layer flow to a turbulent boundary layer when the local Reynolds number on the scale

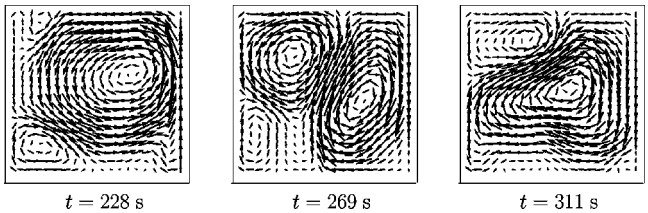

FIG. 13. Velocity patterns at $t=228$, 269, and 311 s for the run in Fig. 12. At $t=228$ s the orientation of the primary eddy is counterclockwise, while at $t=311$ s it is clockwise. At $t=269$ s two large eddies with different orientations can be seen. Here a warmer plume is going upward in the region where the two large eddies collide. It is suppressing the upper counterclockwise eddy.

of ℓ_v at $z \sim \ell_v$ exceeds a value of order 420. Then Nu was claimed to be better expressed by

$$\mathrm{Nu} \sim \mathrm{Ra}^{1/4}(1 + C_1 \mathrm{Ra}^b) \tag{4.5}$$

than by the single power-law form (1.5), where C_1 and b are small coefficient and exponent, respectively, both being of order 0.1. This proposed form of Nu was later claimed to be in good agreement with data [14].

Here it would be informative to add more supplementary explanations of the previous scaling theories. (i) Shraiman and Siggia [2,3] assumed fully developed turbulence in the interior. Then the maximum of the turbulent velocity gradient is of order $S_\mathrm{d} = \eta k_d^2/\rho = (v_\mathrm{pl}^3 \rho / L\eta)^{1/2}$ at the smallest eddy size k_d^{-1} $[\sim (\eta/\rho v_\mathrm{pl})^{3/4} L^{1/4}]$ if the Kolmogorov cascade is assumed with the energy dissipation rate v_pl^3/L [34] (the sparseness of ejected plumes being neglected). If the left-hand side of the sum rule (2.36) is estimated as S_d^2, it follows the relation

$$v_\mathrm{pl} \sim (\mathrm{Pr\ Nu\ Ra})^{1/3} D/L. \tag{4.6}$$

Furthermore, they assumed the linear horizontal velocity profile $v_x \sim (\sigma_0/\eta) z$ in the region $z \lesssim \ell_T \sim L/\mathrm{Nu}$, where σ_0 is given by Eq. (3.17). From the thermal diffusion equation $v_x \partial \delta T/\partial x = D \boldsymbol{\nabla}^2 \delta T$ (the time-dependent fluctuations being neglected), they obtained the scaling,

$$\ell_T^{-3} \sim \rho v_\mathrm{pl}^2 / \eta D L, \tag{4.7}$$

by setting $\partial/\partial x \sim L^{-1}$ and $\boldsymbol{\nabla}^2 \sim (\partial/\partial z)^2 \sim \ell_T^{-2}$ for a cell with $A \sim 1$. From Eqs. (4.6) and (4.7) they found

$$\mathrm{Nu} \sim \mathrm{Pr}^{-1/7}\ \mathrm{Ra}^{2/7}. \tag{4.8}$$

However, as discussed below Eq. (3.14), our simulation suggests that the velocity deviates significantly from the linear profile in the boundary layers. (ii) Castaing *et al.* [5] assumed the balance (4.1) at the length ℓ_T,

$$v_\mathrm{pl} \sim \ell_T^2 g \alpha_p \Delta T/\eta \sim \mathrm{RaNu}^{-2} D/L. \tag{4.9}$$

They further assumed that the typical temperature scale in the interior is $(\delta T)_c \sim v_\mathrm{pl}^2/\alpha_p g L$ and that the average heat current $(\cong \mathrm{Nu}\,\lambda \Delta T/L)$ is of order $C_p (\delta T)_c v_\mathrm{pl}$. From these relations $(\delta T)_c$ may be eliminated to give Eq. (4.6). If we combine Eqs. (4.6) and (4.9), we are again led to Eq. (4.8). Therefore, to justify their arguments, the presence of fully developed turbulence in the interior seems to be required. (iii) Grossmann and Lohse [6,7] estimated the bulk and boundary-layer contributions to the sum rules for the temperature gradient and the velocity gradients, the incompressible version of Eqs. (2.35) and (2.36). Their primary assumption is that the boundary layer thickness for the velocity is given by $\ell_v \sim L/\mathrm{Re}^{1/2}$ in terms of the large-scale Reynolds number Re [34]. Note that this assumption is not consistent with our zeroth-order scaling theory with respect to the Pr dependence. In particular, in the case where $\mathrm{Pr} > 1$ and the boundary-layer contributions are dominant both for the temperature and the velocity, they obtained $\mathrm{Nu} \sim \mathrm{Pr}^{-1/12}\mathrm{Ra}^{1/4}$. In this case we also find $\ell_v/\ell_T \sim \mathrm{Pr}^{1/3}$ from their theory. They predicted that this preturbulent scaling crossovers to the asymptotic turbulent scaling very slowly as in Eq. (4.5).

V. CONCLUDING REMARKS

We have presented a hydrodynamic model of compressible fluids properly taking into account the piston effect and the adiabatic temperature gradient effect. Though performed in two dimensions, our simulation has revealed some important effects in near-critical fluids, such as the overshoot behavior and the amplification of the overall temperature fluctuations as $T \to T_c$. It generally explains the experimental findings [16,17], but a discrepancy remains in the overshoot behavior at high heat flux Q as discussed in Sec. III. It is desirable to extend simulation to smaller ϵ and higher Ra. Also, more experiments on the overshoot and the temperature noises, etc., are needed to resolve the discrepancy and to confirm the new predictions. As by-products, we have numerically examined steady state properties not treated in the previous simulations, such as the logarithmic velocity profile and the random reversal of macroscopic shear flow. They are universal aspects present in both compressible and incompressible fluids.

We have assumed that the fluid is in the supercritical region not very close to the critical point such that the conditions (2.1) and (2.2) are satisfied. However, if ΔT exceeds $T - T_c$ or if T_top is below T_c, we encounter a variety of new effects such as boiling and wetting under heat flow and gravity [23,52]. We believe that such problems should provide us a new challenging field in which nonlinear dynamics and phase transition dynamics are coupled. These problems are beyond the scope of this paper.

ACKNOWLEDGMENTS

We thank H. Meyer for valuable suggestions and comments. Thanks are also due to P. Tong for informative correspondence. This work is supported by Japan Space Forum Grant No. H13-264.

[1] S. Chandrasekhar, *Hydrodynamic and Hydromagnetic Stability* (Clarendon Press, Oxford, 1961).
[2] E. D. Siggia, Annu. Rev. Fluid Mech. **26**, 137 (1994).
[3] B. I. Shraiman and E. D. Siggia, Phys. Rev. A **42**, 3650 (1990).
[4] L. P. Kadanoff, Phys. Today **54**, 34 (2001).
[5] B. Castaing, G. Gunaratne, F. Heslot, L. P. Kadanoff, A. Libchaber, S. Thomae, Xiao-Zhong Wu, S. Zaleski, and G. Zanetti, J. Fluid Mech. **204**, 1 (1989).
[6] S. Grossmann and D. Lohse, J. Fluid Mech. **407**, 27 (2000).
[7] S. Grossmann and D. Lohse, Phys. Rev. Lett. **86**, 3316 (2001).
[8] The usual hydrodynamic equations for one-component fluids in the Boussinesq approximation are valid only when (i) the

fluid is in one-phase states, (ii) the specific heat ratio C_p/C_V is close to 1, (iii) ΔT is much larger than $a_g L$ in Eq. (1.2), and (iv) the gravity-induced stratification is weak such that Eq. (2.2) holds.

[9] M. Sano, Xiao-Zhong Wu, and A. Libchaber, Phys. Rev. A **40**, 6421 (1989).

[10] Xiao-Zhong Wu and A. Libchaber, Phys. Rev. A **45**, 842 (1992).

[11] S. Ashkenazi, Ph.D. thesis, Weizmann Institute of Science, Rehovot, Israel, 1997; S. Ashkenazi and V. Steinberg, Phys. Rev. Lett. **83**, 3641 (1999).

[12] X. Chavanne, Ph.D. thesis, Universiteé Joseph Fourier, Grenoble, 1997.

[13] X. Chavanne, F. Chillà, B. Castaing, B. Hébral, B. Chabaud, and J. Chaussy, Phys. Rev. Lett. **79**, 3648 (1997); X. Chavanne, F. Chillà, B. Chabaud, B. Castaing, and B. Hébral, Phys. Fluids **13**, 1300 (2001).

[14] X. Xu, K. M. S. Bajaj, and G. Ahlers, Phys. Rev. Lett. **84**, 4357 (2000).

[15] G. Ahlers and X. Xu, Phys. Rev. Lett. **86**, 3320 (2001).

[16] A. B. Kogan, D. Murphy, and H. Meyer, Phys. Rev. Lett. **82**, 4635 (1999).

[17] A. B. Kogan and H. Meyer, Phys. Rev. E **63**, 056310 (2001).

[18] J. J. Niemela, L. Skrbek, K. R. Sreenivasan, and R. J. Donnelly, Nature (London) **404**, 837 (2000).

[19] J. J. Niemela, L. Skrbek, K. R. Sreenivasan, and R. J. Donnelly, J. Fluid Mech. **449**, 169 (2001).

[20] B. J. Gluckman, H. Willaime, and J. P. Gollub, Phys. Fluids A **5**, 647 (1993).

[21] S. Cioni, S. Ciliberto, and J. Sommeria, J. Fluid Mech. **335**, 111 (1997).

[22] X.-L. Qiu and P. Tong, Phys. Rev. E **64**, 036304 (2001).

[23] A. Onuki, *Phase Transition Dynamics* (Cambridge University Press, Cambridge, 2002).

[24] A. Onuki and R. A. Ferrell, Physica A **164**, 245 (1990); A. Onuki, H. Hao, and R. A. Ferrell, Phys. Rev. A **41**, 2256 (1990).

[25] J. Straub and K. Nitsche, Fluid Phase Equilib. **88**, 183 (1993); J. Straub, L. Eicher, and A. Haupt, Phys. Rev. E **51**, 5556 (1995).

[26] H. Boukari, J. N. Shaumeyer, M. E. Briggs, and R. W. Gammon, Phys. Rev. A **41**, 2260 (1990).

[27] B. Zappoli, D. Bailly, Y. Garrabos, B. Le Neindre, P. Guenoun, and D. Beysens, Phys. Rev. A **41**, 2264 (1990).

[28] P. Guenoun, B. Khalil, D. Beysens, F. Kammoun, B. le Neindre, Y. Garrabos, and B. Zappoli, Phys. Rev. E **47**, 1531 (1993).

[29] F. Zhong and H. Meyer, Phys. Rev. E **51**, 3223 (1995).

[30] S. Amiroudine, P. Bontoux, P. Larroud, B. Gilly, and B. Zappoli, J. Fluid Mech. **442**, 119 (2001).

[31] Y. Chiwata and A. Onuki, Phys. Rev. Lett. **87**, 144301 (2001).

[32] M. Gitterman and V. Steinberg, J. Appl. Math. Mech. **34**, 305 (1971); M. Gitterman, Rev. Mod. Phys. **50**, 85 (1978).

[33] P. Carlès and B. Ugurtas, Physica D **126**, 69 (1999).

[34] L. D. Landau and E. M. Lifshitz, *Fluid Mechanics* (Pergamon, 1959).

[35] E. E. DeLuca, J. Werne, R. Rosner, and F. Cattaneo, Phys. Rev. Lett. **64**, 2370 (1990); J. Werne, E. E. DeLuca, R. Rosner, and F. Cattaneo, *ibid.* **67**, 3519 (1991).

[36] U. Hansen, D. A. Yuen, and S. E. Kroening, Phys. Fluids A **2**, 2157 (1990); U. Hansen, D. A. Yuen, and A. V. Malevsky, Phys. Rev. A **46**, 4742 (1992). Here the Stokes approximation was used in the range $10^6 < \mathrm{Ra} < 10^9$ in 2D. Nevertheless, they could obtain the scaling (1.5) in agreement with the experiments, which suggests that the balance of the viscous drag and the buoyancy in Eq. (4.1) should have also been realized in the experiments.

[37] S. Balachandar and L. Sirovich, Phys. Fluids A **3**, 919 (1991).

[38] S. Toh and E. Suzuki, *Unstable and Turbulent Motion of Fluid* (World Scientific, Singapore, 1993), p. 272.

[39] C. Bizon, J. Werne, A. A. Predtechensky, K. Julien, W. D. McCormick, J. B. Swift, and H. L. Swinney, Chaos **7**, 107 (1997).

[40] S. L. Christie and J. A. Domaradzki, Phys. Fluids A **5**, 412 (1993).

[41] R. Verzicco and R. Camussi, J. Fluid Mech. **383**, 55 (1999).

[42] R. M. Kerr, J. Fluid Mech. **310**, 139 (1996).

[43] R. M. Kerr and J. R. Herring, J. Fluid Mech. **419**, 325 (2000).

[44] For $0 < \epsilon \ll 1$ the scaling form $\alpha_p = \epsilon^{-\gamma} G(u)$ holds with $u = (\rho/\rho_c - 1)/\epsilon^{\beta}$. For $|u| \ll 1$ or under Eq. (2.2) in gravity, we have $G(u) \cong G(0)$ and $\alpha_p \cong G(0)\epsilon^{-\gamma}$.

[45] G. P. Metcalfe and R. P. Behringer, J. Low Temp. Phys. **78**, 231 (1990).

[46] To be precise, the time constant of the pressure-homogenization is given by $t_{\mathrm{hom}} = (t_{\mathrm{ac}} t_1)^{1/2}$ under the condition $t_{\mathrm{ac}} \ll t_1$ in terms of the acoustic time $t_{\mathrm{ac}} = L/c$ and the piston time t_1 [23]. Here the damping of the pressure oscillation is mainly caused by the damping of the oscillatory heat current in the thermal diffusion layers.

[47] G. Ahlers, M. C. Cross, P. C. Hohenberg, and S. Safran, J. Fluid Mech. **110**, 297 (1981).

[48] L. D. Landau and E. M. Lifshitz, *Statistical Physics* (Pergamon, New York, 1964), Chap. 12. It is well known that the thermal fluctuations of δT and $\delta\rho$ obey the Gaussian distribution proportional to $\exp(-\delta F/k_B T)$, where δF is given by Eq. (2.23). See Ref. [23] for more discussions on this aspect.

[49] A. Schüter, D. Lortz, and F. Busse, J. Fluid Mech. **23**, 129 (1965).

[50] R. P. Behringer and G. Ahlers, Phys. Lett. A **62**, 329 (1977); R. P. Behringer, Rev. Mod. Phys. **57**, 657 (1985). This experiment was performed in ^{4}He at $T = 2.184$ K at saturated vapor pressure. Here the fluid is nearly incompressible and $\gamma_s \cong 1$.

[51] H. Meyer and A. B. Kogan (unpublished).

[52] A. Onuki (unpublished).